Systematic application of the M3Y *NN* forces for describing the capture process in heavy-ion collisions involving deformed target nuclei

I. I. Gontchar ●,[1] M. V. Chushnyakova ●,[2] and O. M. Sukhareva ●[2,*]

[1]*Department of Physics and Chemistry, Omsk State Transport University, 644046 Omsk, Russia*
[2]*Department of Physics, Omsk State Technical University, 644050 Omsk, Russia*

We present results of a systematic study of the capture process through the barrier penetration model. The nucleus-nucleus interaction potential is calculated using the double-folding model (DFM) with the M3Y Paris *NN* forces. The nucleon densities entering the model are generated from the experimental three-parameter Fermi charge densities. The DFM has been extended to the case of deformed target nuclei. It is shown that the density-dependent M3Y *NN* forces with the finite range exchange part can be mimicked successfully by the zero-range density-independent forces. The latter option significantly reduces the required computer time. For the nucleon densities and target nuclei deformations, we employ the values from the commonly used data bases. Thus, we do not vary any parameters to reach a better agreement with the data. The resulting cross sections are compared with data for 20 reactions with the product of the charge numbers $Z_P Z_T$ ranging from 216 up to 2576. We discuss the opinion met in the literature that the M3Y *NN* forces provide a poorer description of the capture cross sections in heavy-ion collisions in comparison to the *NN* forces coming from the relativistic mean-field approach. Our calculations show that the M3Y *NN* forces give an agreement with the data which is not perfect yet is not worse than the one resulting from the relativistic mean-field approach *NN* forces.

I. INTRODUCTION

The optical model is known to be one of the best tools for describing collisions of heavy ions including the coupled channels. The nucleus-nucleus potential entering the optical model is often based on the effective *NN* forces [1]. For this aim, the single folding approach was first developed for the case of proton impinging on a nucleus [2]. Later, this approach was generalized for the case of two complex colliding nuclei becoming the double-folding model (DFM) [3,4]. Since then, the DFM has been used widely for finding the real part of the optical potential and the Coulomb barriers (see, e.g., Refs. [5–8]).

For the *NN* forces, in the nonrelativistic approximation, three versions are typically used. These are the zero-range Migdal forces [3,9] and two kinds of the Yukawa-type M3Y forces: the Reid forces [6,10], and the Paris forces [11]. For calculating the capture cross sections, the use of the Reid forces in comparison with the Paris forces was studied in Ref. [12], whereas the comparison between the Migdal and the M3Y Paris forces in the same context was performed in Refs. [13,14].

Recently, the Yukawa-type *NN* forces coming from the relativistic mean-field approach [(RMF) *NN* forces] were applied for calculating the fusion cross sections of heavy ions [15–17]. In Refs. [15,16], it was claimed that the RMF *NN* forces provide " ... a better choice than the M3Y interaction for fusion reaction considered in the entire range of barrier energies in

predicting the cross sections … ." The purpose of the present paper is to confirm or disprove this statement. For this goal, using the DFM, we calculated the capture cross sections for 20 reactions involving the deformed target nuclei. This model is described in Sec. II for the M3Y and RMF *NN* forces. The logic of our calculations with the M3Y *NN* forces is presented in Sec. III. In Sec. IV, the choice of reactions is explained. The nucleon densities entering the DFM are discussed in Sec. V. In Sec. VI, the cross sections resulting from the M3Y Paris *NN* forces are compared with the experimental data and with the cross sections of Ref. [15] resulting from the RMF *NN* forces. The conclusions are formulated in Sec. VII. The Appendix contains the details of the DFM calculations for the case of the deformed target nucleus.

II. THE DOUBLE-FOLDING MODEL

Within the framework of the DFM, the strong nucleus-nucleus potential (SnnP) $U_n(\vec{R})$ comprises two parts, the direct $U_{nD}(\vec{R})$ and the exchange $U_{nE}(\vec{R})$ ones,

$$U_n(\vec{R}) = U_{nD}(\vec{R}) + U_{nE}(\vec{R}). \quad (1)$$

The vector $\vec{R}$ connects the centers of mass of the colliding nuclei. The direct part is evaluated as follows:

$$U_{nD}(\vec{R}) = \int d\vec{r}_P \int d\vec{r}_T \rho_{AP}(\vec{r}_P) F(\rho_{FA}) v_D(s) \rho_{AT}(\vec{r}_T). \quad (2)$$

Here $\vec{r}_P$ and $\vec{r}_T$ are the radius vectors of the interacting points of the projectile (*P*) and target (*T*) nuclei. The distance between these points is defined by the vector $\vec{s} = \vec{r}_T - \vec{R} - \vec{r}_P$. The geometry of the collision and all these vectors are shown
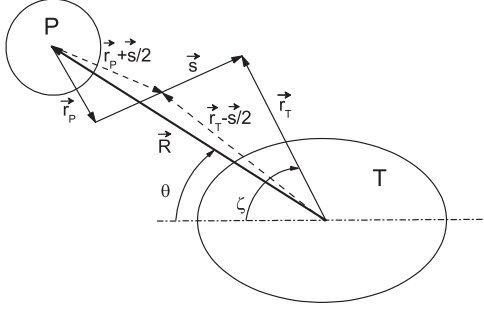
*o.m.sukhareva@gmail.com

FIG. 1. Coordinate system used in the double-folding model.

in Fig. 1. In Eq. (2), ρ_{AP} and ρ_{AT} represent the nucleon densities (diagonal components of the density matrices) for the projectile and target nuclei, respectively. The multiplier $F(\rho_{FA})$ represents the density dependence of the NN forces and is the same for both direct and exchange parts. For the case of two spherical colliding nuclei, it reads [18]

$$F(\rho_{FA}) = 0.3429\{1 + 3.0232 \exp(-\beta \rho_{FA}) - \gamma \rho_{FA}\}, \quad (3)$$

$\beta = 3.5512 \, \text{fm}^3$, $\gamma = 0.5 \, \text{fm}^3$. This parameter set results in the lowest barrier (see Ref. [12] for details). The nucleon density ρ_{FA} in Eq. (2) reads [19]

$$\rho_{FA} = \rho_{AP}(r_P) + \rho_{AT}(r_T). \quad (4)$$

This choice is dictated more by numerical convenience than by physical arguments.

The direct part of the NN forces comprises two Yukawa terms,

$$v_D(s) = \sum_{i=1}^{2} G_{Di} \frac{\exp(-s/r_{vi})}{s/r_{vi}}. \quad (5)$$

Parameters of the NN forces are presented in Table I. In the present paper, we discuss only M3Y Paris forces calling them the NN forces.

The exchange part of the SnnP reads

$$U_{nE}(\vec{R}) = \int d\vec{r}_P \int d\vec{r}_T \hat{\rho}_{AP}(\vec{r}_P; \vec{r}_P + \vec{s}) \, F(\rho_{FA}) \, v_E(s)$$
$$\times \hat{\rho}_{AT}(\vec{r}_T; \vec{r}_T - \vec{s}) \exp(i\vec{k}_{rel}\vec{s} \, m_n/m_R). \quad (6)$$

TABLE I. Parameter set for the effective M3Y Paris NN forces. The coefficients G_{Di} and G_{Efi} were obtained by fitting the G-matrix elements at three selected distances r_{vi}.

Parameter	Value
G_{D1} (MeV)	11062
G_{D2} (MeV)	-2537.5
G_{Ef1} (MeV)	-1524.25
G_{Ef2} (MeV)	-518.75
G_{Ef3} (MeV)	-7.847
$G_{E\delta0}$ (MeV fm^3)	-592
r_{v1} (fm)	0.25
r_{v2} (fm)	0.40
r_{v3} (fm)	1.414

Here m_R is the reduced mass; $\hat{\rho}_{AP}$ ($\hat{\rho}_{AT}$) is the nondiagonal matrix element for the projectile (target) nucleus. These elements are evaluated using the density-matrix expansion method of Refs. [20,21],

$$\hat{\rho}_{AT}(\vec{r}_T; \vec{r}_T - \vec{s}) \approx \rho_{AT}(\vec{r}_T - \vec{s}/2) \tilde{j}_1[k_{\text{eff}}(\vec{r}_T - \vec{s}/2) \, s], \quad (7)$$

$$\hat{\rho}_{AP}(\vec{r}_P; \vec{r}_P + \vec{s}) \approx \rho_{AP}(\vec{r}_P + \vec{s}/2) \tilde{j}_1[k_{\text{eff}}(\vec{r}_P + \vec{s}/2) \, s], \quad (8)$$

$$\tilde{j}_1(x) = 3[\sin(x) - x \cos(x)]/x^3. \quad (9)$$

For the effective Fermi momentum k_{eff}, we apply the simplest Slater approximation,

$$k_{\text{eff}}(\vec{r}) = \left[\frac{3\pi^2 \rho_A(\vec{r})}{2}\right]^{2/3}. \quad (10)$$

The nucleon density ρ_{FA} in Eq. (6) reads [6,18,22]

$$\rho_{FA} = \rho_{AP}\left(\left|\vec{r}_P + \frac{\vec{s}}{2}\right|\right) + \rho_{AT}\left(\left|\vec{r}_T - \frac{\vec{s}}{2}\right|\right). \quad (11)$$

This corresponds to the middle point between the interacting points of the projectile and the target nuclei and is physically justified (see Fig. 1).

The wave number corresponding to the relative motion of the colliding nuclei k_{rel}, reads

$$k_{rel}(\vec{R}) = \sqrt{2m_R [E_{c.m.} - U_n(\vec{R}) - U_C(\vec{R})]}/\hbar. \quad (12)$$

Here $E_{c.m.}$ is the collision energy and $U_C(\vec{R})$ is the Coulomb interaction energy. The total effective interaction energy of the colliding nuclei $U(\vec{R})$ including in addition the centrifugal (rotational) energy $U_{rot}(\vec{R})$ reads

$$U(\vec{R}) = U_n(\vec{R}) + U_C(\vec{R}) + U_{rot}(\vec{R}). \quad (13)$$

The exchange part of the NN forces $v_E(s)$ is met in the literature in two versions: with zero range and with finite (nonzero) range. Let us denote the former one as δNN forces and the latter one as fNN forces. The simpler δNN forces read

$$v_{E\delta}(s) = G_{E\delta} \, \delta(\vec{s}). \quad (14)$$

In this case, the nondiagonal matrix elements in Eq. (6) are reduced to the diagonal elements and the integrals take the form of Eq. (2). Such integrals are evaluated rather fast by means of the Fourier transform (see details in Refs. [22–24]). Since in the present paper we will modify $G_{E\delta}$, we denote the original value corresponding to Ref. [11] as $G_{E\delta0}$.

The much more sophisticated fNN forces involve three Yukawa terms,

$$v_{Ef}(s) = \sum_{i=1}^{3} G_{Efi} \frac{\exp(-s/r_{vi})}{s/r_{vi}}. \quad (15)$$

In this case, evaluating the integrals in Eq. (6) is significantly more computer time consuming. The required computer time dramatically increases even more when one deals with the deformed target nucleus because one needs to evaluate the integrals (6) many times for many values of R and θ (see Fig. 1). On the other hand, only the fNN density-dependent forces ($fDDNN$ forces) provide the correct saturated nucleon density for cold nuclear matter [18]. Moreover, the $fDDNN$ forces have been applied only to the case of spherical colliding

nuclei [4,12,19,25–29] whereas, in the present paper, we aim to study the reactions with deformed target nuclei.

In addition, we would like to compare our results with the calculations obtained in Ref. [15] within the DFM with the RMF *NN* forces. It has the same structure as in the case of M3Y *NN* forces. Most of the differences come from the way the *NN* forces are obtained. Starting from the standard Lagrangian density [15,30], the effective RMF *NN* interaction is constructed in the form of the Yukawa-type terms [15,17,31–33],

$$v_{\mathrm{RMF}}(r) = \frac{g_\omega^2}{4\pi} \frac{\exp\left(-m_\omega rc/\hbar\right)}{r} + \frac{g_\rho^2}{4\pi} \frac{\exp\left(-m_\rho rc/\hbar\right)}{r}$$
$$- \frac{g_\sigma^2}{4\pi} \frac{\exp\left(-m_\sigma rc/\hbar\right)}{r} + \frac{g_2^2}{4\pi} r \exp\left(-2m_\sigma rc/\hbar\right)$$
$$+ \frac{g_3^2}{4\pi} \frac{\exp\left(-3m_\sigma rc/\hbar\right)}{r} - J_{00}\delta(\vec{r}). \quad (16)$$

The free parameters of this theory, the meson masses m_ρ, m_σ, m_ω, and the interaction strengths g_ρ, g_σ, g_ω, g_2, g_3 are fitted to reproduce the static properties of the nuclei.

Thus, although formally similar, the M3Y and RMF *NN* forces come from different considerations. Moreover, the strength of the zero-range potential in the M3Y forces [Eqs. (14), (A12)] was scaled to reproduce the exchange integral of the potential obtained with the finite-range exchange term of the M3Y interaction. This has nothing to do with the effective interaction derived from RMF. Therefore, adding the last δ-function term in Eq. (16) as it was performed in Refs. [15,16,33] seems to be questionable.

Moreover, the coupling strengths of different mesons in the RMF were carefully chosen to describe the saturation of nuclear matter as well as the ground-state structure of some nuclei. Therefore, the single nucleon exchange effects are already accounted for implicitly. It looks like adding by hand a zero-range potential to the in-medium *NN* interaction derived from the RMF meson fields is a sort of double counting. Note that in Refs. [31,32] the zero-range pseudopotential is absent.

These effective forces are folded with the densities analogously to Eq. (2). It should be noted that the RMF *NN* forces were applied in the literature only for the case of spherical target and projectile nuclei. Therefore, the SnnP reads

$$U_n(R) = \int d\vec{r}_P \int d\vec{r}_T \rho_{AP}(r_P) v_{\mathrm{RMF}}(s) \rho_{AT}(r_T). \quad (17)$$

III. COMPUTATIONAL ROUTINE

In our investigation, we use two computer codes: DFMSPH [24,34] and DFMDEF [35,36] (see details of the DFMDEF code in the Appendix). The first one is designed for calculating the interaction energy of two spherical colliding nuclei and allows accounting for the density dependence of *NN* forces. It was shown in Refs. [18,25] that only density-dependent M3Y *NN* forces with the finite range exchange term allow reproducing the saturation density of cold nuclear matter. Within the framework of DFMDEF, one can calculate the interaction energy of a spherical projectile nucleus and a deformed target nucleus.

Note that in both DFMSPH and DFMDEF there is an option for treating the single-nucleon exchange in a local approximation using the finite-range exchange part of the M3Y interaction which was proven to be a much more accurate procedure compared to the zero-range pseudopotential.

However, the density dependence of the *NN* forces is absent in the DFMDEF code. To account for this density dependence in an approximate manner for the reactions with deformed target nuclei and simultaneously to reduce the computer time needed for the systematic calculations, we have developed the following algorithm.

We start from finding the barrier energies through DFMSPH (i.e., ignoring the target nucleus deformation) using the fDD*NN* forces. The corresponding barrier energies are denoted $B_{f\mathrm{DD}s}$ (the last "s" in the subscript stands for "spherical"). Next, we apply the δNN density-independent forces and, varying $G_{E\delta}$, fit the Coulomb barrier energies $B_{f\mathrm{DD}s}$. Let us denote this fitting barrier energy as $B_{\delta s}$ and the corresponding value of $G_{E\delta}$ as $G_{E\delta s}$. Then, we evaluate the θ-dependent SnnP and the barrier energy $B_\delta(\theta)$ with this optimal value $G_{E\delta s}$, accounting for the deformation of the target nucleus using the code DFMDEF. These are the SnnP and barrier energy we plan to apply for calculating the cross sections.

To verify that the resulting barrier energies $B_\delta(\theta)$ answer our purpose, we compare them with the barrier energies calculated with $f NN$ forces. For this aim, we evaluate the incident angle-dependent barrier energies $B_f(\theta)$ using the code DFMDEF accounting for the deformations of the target nucleus. Since the density dependence is absent in DFMDEF, we need to find a correcting factor responsible for the contribution of the density dependence. This factor comes from the comparison of $B_{f\mathrm{DD}s}$ and B_{fs} calculated for spherical nuclei within DFMSPH using the $f NN$ forces with density dependence and without it, respectively. Thus, we obtain the corrected barrier energies $B_{fc}(\theta)$. We expect good agreement between the simplified barrier energy $B_\delta(\theta)$ and the more rigorous $B_{fc}(\theta)$.

Note that a similar contrivance, proposed in Ref. [37], was successful but did not receive further development. In the present paper, we work out that idea.

IV. SELECTING THE REACTIONS

The nuclei and reactions for the present paper have been selected according to the following considerations. First, we tried selecting the reactions in which a smaller spherical projectile nucleus collides with a significantly bigger deformed target nucleus. Second, we used only those nuclei for which in Ref. [38] the three-parameter Fermi functions (3pF formulas) are available for the experimental charge density. Third, the reactions have been chosen to cover a wide range of the approximate Coulomb barrier,

$$B_Z = \frac{Z_P Z_T}{A_P^{1/3} + A_T^{1/3}} \text{ MeV}. \quad (18)$$

Fourth, we selected the target nuclei possessing significant quadrupole and hexadecapole deformations of both signs.

Finally, we prefer the reactions for which experimental data on the barrier energy and/or capture cross sections are available. Many data are taken from the database [39].

Information on the projectile and target nuclei is composed in Tables II and III, respectively; the reactions selected for consideration in the present paper are composed in Table IV. Even when the projectile nucleus is known to be deformed, we consider it as spherical one. This does not wrench our results due to the smaller size of the projectile nucleus.

The present paper has a lot in common with Ref. [37]. Here comes the list of the differences: (i) in the present paper, we significantly widen the range of reactions considered (20 against 7); (ii) reactions with ^{168}Er and ^{12}C are excluded because the parameters of the 3pF formulas for the experimental charge densities of these nuclei are absent; (iii) the approximation for the finite-range calculations are performed here for all 20 reactions. In addition, in Ref. [37], contrary to the present paper, the calculated capture cross sections were not presented. On the other hand, the details of the calculations omitted here can be found in Refs. [36,37].

V. NUCLEON DENSITIES

Basing on the experimental charge densities from Ref. [38], we approximate the nucleon densities for spherical nuclei by the 3pF formula,

$$\rho_F(r) = \rho_{CF} \frac{1 - w_F r^2/R_F^2}{1 + \exp[(r - R_F)/a_F]}. \quad (19)$$

Here a_F denotes the diffuseness of the density, R_F approximately corresponds to the half-density radius. The quantity w_F seems not to have a specific name in the literature. The value of ρ_{CF} is defined by the normalization condition. In Ref. [38], Eq. (19) is applied for the nuclear charge density of both spherical and deformed nuclei. In the latter case, the average over the polar angle ζ (see Fig. 1) is meant. Note that the two-parameter Fermi function formula used in Ref. [38] is just the same 3pF formula with $w_F = 0$.

The SnnP of the colliding nuclei significantly depends upon the incident angle θ. Therefore, when dealing with the deformed nucleus, we use the following dependence upon ζ:

$$\rho_F(r, \zeta) = \rho_{CF}(1 + \exp\{[r - R_F f(\zeta)]/a_F\})^{-1}, \quad (20)$$

$$f(\zeta) = \lambda^{-1}[1 + \beta_2 Y_{20}(\zeta) + \beta_4 Y_{40}(\zeta)]. \quad (21)$$

Here β_2 and β_4 are the parameters of the quadrupole and hexadecapole deformations, respectively, whose values for the target nuclei were taken from Ref. [40], λ guarantees the nucleon number conservation; $Y_{20}(\zeta)$ and $Y_{40}(\zeta)$ denote the spherical functions.

The same formulas (19) and (20) are used for the charge, neutron, and proton densities. The half-density radii are the same for a given nucleus whereas the diffusenesses of proton a_{Fp} and neutron a_{Fn} densities are extracted from the experimental diffuseness a_{Fq} of the charge density [1,37],

$$a_{Fp} = a_{Fn} = \sqrt{a_{Fq}^2 - \frac{5}{7\pi^2}\left(0.76 - 0.11\frac{N}{Z}\right)}. \quad (22)$$

In the present paper, the densities are considered to be frozen. This frozen density approximation (FDA) has been inspected carefully and compared with the adiabatic density approximation (ADA) in Ref. [41]. The ADA has been shown to be more appropriate at smaller center-to-center distances, in other words, at larger densities overlap. We will come back to this point in Sec. VI A below.

VI. RESULTS

A. Barrier energies ignoring target deformations

All calculations in this subsection are performed through the code DFMSPH. According to the formulated algorithm, we present in this subsection the barrier energies $B_{f\mathrm{DD}s}$ calculated using the fDDNN forces but ignoring the deformations of the target nuclei. The values of $B_{f\mathrm{DD}s}$ are shown in Table IV.

Next, we have calculated the barrier energies $B_{\delta s}$ using the δNN forces with several values of $G_{E\delta}$ also ignoring the deformations of the target nuclei. It is convenient representing the results using the fractional difference,

$$\xi_{\delta D}^s(B_Z) = \frac{B_{\delta s}}{B_{f\mathrm{DD}s}} - 1. \quad (23)$$

These differences calculated at three values of $G_{E\delta} = -940$, -1040, and -1140 MeV fm^3 are plotted in Fig. 2(a). This figure shows that the value $G_{E\delta s} = -1040$ MeV fm^3 can be taken as an optimal one for all the reactions considered. We apply this value below calling this version of calculations "modified δNN forces."

Let us now compare the barrier energies evaluated accounting for the density dependence $B_{f\mathrm{DD}s}$ and without this dependence B_{fs}. This comparison is presented in Fig. 2(b) as the fractional difference,

$$\xi_{fD}^s(B_Z) = \frac{B_{fs}}{B_{f\mathrm{DD}s}} - 1. \quad (24)$$

On average, this fractional difference is about 1% (thin horizontal line), however, it reveals a tendency to increase at small values of B_Z and to flatten at larger values of B_Z. Below we use ξ_{fD}^s for finding a proper correcting factor for the deformed barriers. Therefore, we prefer to approximate the $\xi_{fD}^s(B_Z)$ dependence by the following analytical expression:

$$\xi_a(B_Z) = \xi_1 \exp\left(\frac{B_0 - B_Z}{\Delta B}\right) + \xi_0. \quad (25)$$

In Fig. 2(b), ξ_a calculated with $\xi_0 = 0.80$, $\xi_1 = 0.50$, $B_0 = 40$ MeV, and $\Delta B = 15$ MeV is shown by the curved line.

Probably, it is worthwhile to inspect whether the FDA makes sense for the presented calculations. For this aim, we display in Fig. 3 the fractional difference,

$$\mu_R(B_Z) = \frac{R_{Bfs}}{R_{FP} + R_{FT}} - 1 \quad (26)$$

showing to what extent the spherical barrier radius calculated using the fDDNN forces R_{Bfs} is larger than the sum of half-density radii of the projectile R_{FP} and target R_{FT} nuclei. This fractional difference typically exceeds 20%, thus, the FDA seems to be justified.
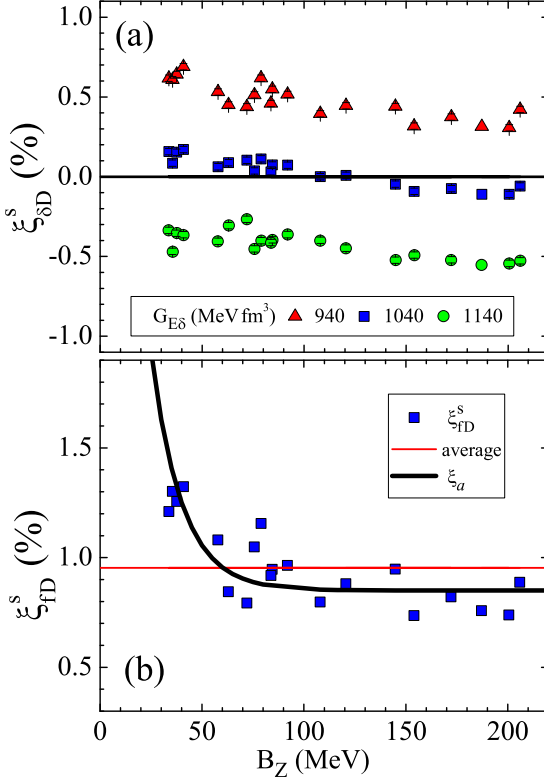
FIG. 2. Comparison of barrier energies evaluated ignoring the deformations of the target nuclei versus the approximate barrier energy B_Z. In panel (a) fractional difference $\xi_{\delta D}^s$ [see Eq. (23)] corresponds to three values of $G_{E\delta}$ indicated in the panel. In panel (b) squares correspond to fractional difference ξ_{fD}^s [see Eq. (24)]; thin horizontal line is the average of $\xi_{fD}^s(B_Z)$; thick black curve is the analytical approximation $\xi_a(B_Z)$ [see Eq. (25)].

B. Barrier energies accounting for target deformations

All calculations in this subsection are performed within the framework of the code DFMDEF. We now evaluate the barrier energies $B_\delta(\theta)$ accounting for the deformations of
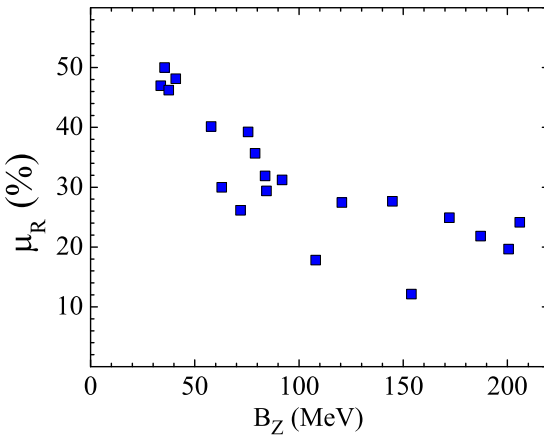

FIG. 3. Excess of the spherical barrier radius calculated using the fDDNN forces R_{Bfs} over the sum of half-density radii of the projectile R_{FP} and target R_{FT} nuclei versus B_Z [see Eq. (26)].
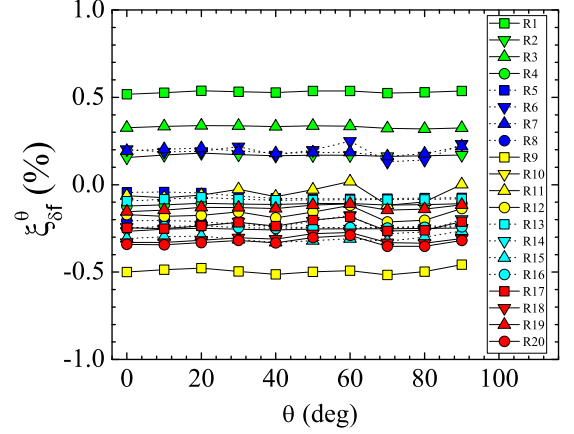

FIG. 4. Fractional difference $\xi_{\delta f}^\theta(\theta)$ [see Eq. (28)] versus accident angle θ. For convenience, we use the ordering numbers of reactions from Table IV.

the target nuclei as indicated in Table III. These energies are calculated using the modified δNN forces, i.e., with the optimal value $G_{E\delta s}$ chosen in the previous subsection. Since the value of $G_{E\delta s}$ was found by basing on the calculations with density-dependent forces, it implicitly includes this dependence. These are the calculations we intend to apply for the capture cross-sectional calculations. However, first we would like to test if the values of $B_\delta(\theta)$ indeed correspond to the barriers with finite-range NN forces. Therefore, we calculate $B_f(\theta)$ and correct them using the correcting factor $\xi_a(B_Z)$ of Eq. (25) as follows:

$$B_{fc}(\theta,\, B_Z) = \frac{B_f(\theta, B_Z)}{1 + \xi_a(B_Z)}. \tag{27}$$

This procedure is extremely computer time consuming; therefore, it is performed for several values of θ only. These barrier energies B_{fc} are compared with $B_\delta(\theta)$ via the fractional
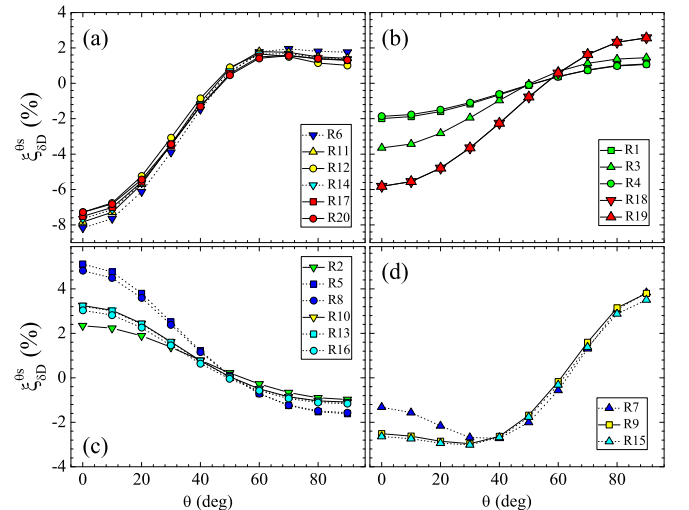

FIG. 5. Fractional difference $\xi_{\delta D}^{\theta s}(\theta)$ [see Eq. (29)] as a function of accident angle θ.

TABLE II. Projectile nuclei: parameters of the experimental charge density [3pF formula, Eq. (19)] [38].

	^{16}O	^{19}F	^{20}Ne	^{26}Mg	^{27}Al	^{40}Ar	^{48}Ti	^{56}Fe	^{58}Ni	^{64}Ni
R_F (fm)	2.608	2.590	2.805	3.050	3.070	3.530	3.843	4.106	4.309	4.212
a_F (fm)	0.513	0.564	0.571	0.523	0.519	0.542	0.588	0.519	0.517	0.578
w_F	−0.051	0.000	0.000	0.000	0.000	0.000	0.000	0.000	−0.131	0.000

difference,

$$\xi_{\delta f}^{\theta}(\theta) = \frac{B_{\delta}(\theta)}{B_{fc}(\theta)} - 1. \tag{28}$$

Results for all 20 reactions from Table IV are presented in Fig. 4. The deviation of the simplified barrier energies $B_{\delta}(\theta)$ from the more rigorous $B_{fc}(\theta)$ is within 0.5% for all values of the incident angle and B_Z. Thus, we believe it is justified to utilize the SnnP $U_n(R, \theta)$ with δNN forces corresponding to the optimal value $G_{E\delta s}$ for calculating the total effective interaction energy of the colliding nuclei $U(R, \theta)$ and for evaluating the capture cross sections.

Before doing that, we wish to discuss shortly a side result of our paper, namely, the scaling properties of the barrier energies $B_{\delta}(\theta)$. For this aim, we present in Fig. 5 one more fractional difference,

$$\xi_{\delta D}^{\theta s}(\theta) = \frac{B_{\delta}(\theta)}{B_{fDDs}} - 1. \tag{29}$$

In this figure, all reactions are split into four groups according to the deformations of the target nuclei: Figure 5(a) comprises the cases of significant and positive β_2 and β_4; in Fig. 5(b), both β_2 and β_4 are positive, but β_4 is small; in Fig. 5(c) the cases of significant negative β_2 are collected; finally, the remaining reactions are shown in Fig. 5(d). For convenience, we use the ordering numbers of reactions from Table IV. The first group is formed by the reactions with samarium, thorium, and uranium as the target nuclei whose quadrupole and hexadecapole deformations are close according to Table III. As the consequence, the curves in Fig. 5(a) are hardly distinguishable. Note that the absolute values of the spherical barrier energies for these reactions are quite different: from 60.6 MeV for reaction $R6$ up to 205.0 MeV for $R20$. Here the shape of $\xi_{\delta D}^{\theta s}(\theta)$ is defined by the prolate shape of the nucleus. Note that the barrier at the pole is 8% lower than the spherical barrier. This must dramatically influence the capture excitation function at the barrier region. Therefore, results of Ref. [16] where ^{238}U and ^{246}Cm were considered to be spherical seem to be unreliable.

Figure 5(b) comprises the fractional differences $\xi_{\delta D}^{\theta s}(\theta)$ for reactions involving holmium, cobalt, and chromium target nuclei whose hexadecapole deformations are much smaller than for the first group. Accordingly, the range of $\xi_{\delta D}^{\theta s}(\theta)$ is here much narrower than in Fig. 5(a). This range is especially narrow for reactions $R1$ and $R4$ involving ^{59}Co in agreement with its comparatively small quadrupole deformation. Yet anyway the pole barrier energies are smaller than the equator ones.

The situation changes strikingly in Fig. 5(c) due to the opposite sign of both β_2 and β_4. Due to the oblate shape of copper, germanium, and gold nuclei, the polar barrier energies are now higher than the equatorial ones.

After the above analysis, Fig. 5(d) seems to be self-explanatory. A general conclusion from Fig. 5 is that the fractional difference $\xi_{\delta D}^{\theta s}(\theta)$ depends solely upon the deformations of the target nucleus. This circumstance can probably help in extracting the values of β_2 and β_4 from the experimental data.

C. Capture cross sections: qualitative comparison with the data

Following Refs. [37,49,71], we evaluate the capture cross section as:

$$\sigma_{th} = \frac{\pi \hbar^2}{2m_R E_{\text{c.m.}}} \sum_i \sum_J (2J + 1) T_J(\theta_i) \sin(\theta_i) \Delta\theta. \tag{30}$$

Here, J is the angular momentum in units of $\hbar$. This semiclassical approach provides results that are close to the exact quantum-mechanical calculations [71,72]. The transmission coefficient is calculated using the Wentzel-Kramers-Brillouin approximation below the barrier,

$$T_J(\theta) = \left\{ 1 + \exp\left[\frac{2S}{\hbar}\right] \right\}^{-1}, \tag{31}$$

and in the parabolic barrier approximation above the barrier,

$$T_J(\theta) = \{1 + \exp[2\pi(B_{\delta} - E_{\text{c.m.}})/(\hbar\omega_B)]\}^{-1}. \tag{32}$$

TABLE III. Target nuclei: deformations [39,40] and parameters of the experimental charge density [3pF formula, Eqs. (20) and (21)] [38].

	^{50}Cr	^{59}Co	^{65}Cu	^{74}Ge	^{154}Sm	^{165}Ho	^{181}Ta	^{186}W	^{197}Au	^{232}Th	^{238}U
β_2	+0.194	+0.118	−0.125	−0.237	+0.270	+0.284	+0.255	+0.221	−0.125	+0.205	+0.236
β_4	+0.038	+0.005	−0.005	−0.036	+0.105	+0.020	−0.076	−0.095	−0.017	+0.103	+0.098
R_F (fm)	3.979	4.080	4.158	4.450	5.939	6.180	6.380	6.580	5.380	6.792	6.805
a_F (fm)	0.520	0.569	0.632	0.580	0.522	0.570	0.640	0.480	0.535	0.571	0.605

TABLE IV. The ordering numbers of reactions, the corresponding reactions, and the barrier energies: the approximate ones B_Z [Eq. (18)]; $B_{\delta s}$ calculated using the δNN forces with $G_{E\delta} = -1040$ MeV fm^3; B_{fDDs} evaluated using the fDDNN forces; the experimental ones $B_{f\,\exp}$ with the corresponding references. In the last column, the references for the experimental capture cross sections, and the number of experimental points are presented.

	Reaction	B_Z (MeV)	$B_{\delta s}$ (MeV)	B_{fDDs} (MeV)	$B_{f\,\exp}$ (MeV), Reference	Number of points, capture data
R1	^{16}O + ^{59}Co	33.68	29.56	29.51	30.5 [42]	4 [42], 2 [43]
R2	^{16}O + ^{65}Cu	35.47	30.66	30.63		9 [44], 7 [45]
R3	^{20}Ne + ^{50}Cr	37.51	32.51	32.46		3 [46]
R4	^{20}Ne + ^{59}Co	40.86	35.55	35.49		10 [47]
R5	^{27}Al + ^{74}Ge	57.79	53.14	53.10	55.2 [48]	18 [48]
R6	^{16}O + ^{154}Sm	62.94	60.61	60.56	59.4 [49]	39 [49], 22 [50]
R7	^{16}O + ^{186}W	71.95	69.54	69.47	59.35 [51]	38 [52]
R8	^{40}Ar + ^{74}Ge	75.61	70.82	70.79		3 [53]
R9	^{19}F + ^{181}Ta	78.92	72.94	72.86		10 [54], 9 [55], 8 [56]
R10	^{19}F + ^{197}Au	83.77	81.42	81.40	81.61 [51]	8 [57]
R11	^{16}O + ^{238}U	84.43	81.91	81.85	85 [58]	4 [59], 2 [60]
R12	^{19}F + ^{232}Th	91.91	89.23	89.17	89.30 [51]	15 [61], 6 [62]
R13	^{26}Mg + ^{197}Au	107.96	107.46	107.46		1 [63]
R14	^{26}Mg + ^{238}U	120.53	119.09	119.08	123 [58]	3 [63]
R15	^{40}Ar + ^{181}Ta	144.77	140.29	140.35		6 [64]
R16	^{40}Ar + ^{197}Au	153.92	156.28	156.43		3 [65], 3 [66], 5 [67]
R17	^{40}Ar + ^{238}U	172.19	173.61	173.74		3 [66], 2 [68]
R18	^{56}Fe + ^{165}Ho	187.10	188.20	188.40		4 [69]
R19	^{58}Ni + ^{165}Ho	200.52	202.47	202.69		2 [70]
R20	^{48}Ti + ^{238}U	205.87	206.90	207.02		1 [60]

In Eq. (31), S denotes the action calculated from the outer down to the inner turning points. In Eq. (32), both the barrier energy B_δ and the frequency ω_B are J and θ dependent. The incident angle changes with step $\Delta\theta = 2.5°$ from $0°$ up to $90°$ due to the mirror symmetry of the target nuclei. The summation over J is terminated when the partial cross section becomes 10^{-5} of its maximum value.

The capture excitation functions have been calculated and compared with the data for all 20 reactions. The problem is that for many reactions only several experimental points of the excitation functions are available (see the last column of Table IV). Therefore, we have selected for the detailed presentation six reactions for which the experimental capture cross-sections $\sigma_{\exp}$ obey three conditions: (i) they should cover a rather wide range of B_Z, (ii) a reasonable number of experimental points should be available, (iii) for a given reaction the data should cover the barrier energy region. These data and calculated cross-sections σ_{th} are presented in Fig. 6 [panels (a) and (b) provide the cross sections in linear and logarithmic scales, respectively]. In all cases but one, the calculated cross sections lay below the data in the sub-barrier region and above the data at $E_{\text{c.m.}} > B_{\delta s}$. For the reactions not shown in Fig. 6, the mutual layout of $\sigma_{\exp}$ and σ_{th} do not contradict this with very few exceptions.

We interpret this observation in the following way. At $E_{\text{c.m.}} > B_{\delta s}$, the collisions become strongly dissipative and require including friction to be modelled correctly. This had been performed before in many works [17,27–29,73–76]. Including dissipation within dynamical calculations can help to bring the theoretical above-barrier cross sections in agreement with the data. Below the barrier, dissipation probably plays a minor role in comparison with the SnnP.

However, there is one more uncertainty: the deformation of the target nucleus. Here, we utilize the theoretical deformation parameters from Ref. [40] which are not always in agreement with the experimental values. For instance, for spherical ^{16}O, Ref. [40] predicts $\beta_3 = -0.258$ and $\beta_4 = -0.122$. An alternative would be to use the experimental deformations in our calculations. Unfortunately, these data are not available for all target nuclei.

D. Capture cross sections: quantitative comparison with the data

To compare the calculated cross-sections σ_{th}(M3Y) with the experimental ones more quantitatively, we collect their ratios for all analyzed reactions in Fig. 7 [in linear and log-arithmic scales in panels (a) and (c), respectively] as the functions of $E_{\text{c.m.}}/B_Z$. Since the present research is motivated by the statement of Ref. [15] that the RMF NN forces provide " … a better choice than the M3Y interaction for fusion reaction considered in the entire range of barrier energies in predicting the cross sections …," in parallel, the same ratios extracted from that paper are presented in Figs. 7(b) and 7(d). Note that in Ref. [15], only two narrow ranges of B_Z were considered: 98–101 and 154–158 MeV whereas in our analysis $34 < B_Z/\text{MeV} < 206$ (see Table IV). This circumstance explains the more scattered behavior of the points in Figs. 7(a) and 7(c). In contrast to the conclusions of the authors of Ref. [15], we do not see any superiority of the calculations performed with the RMF NN forces.
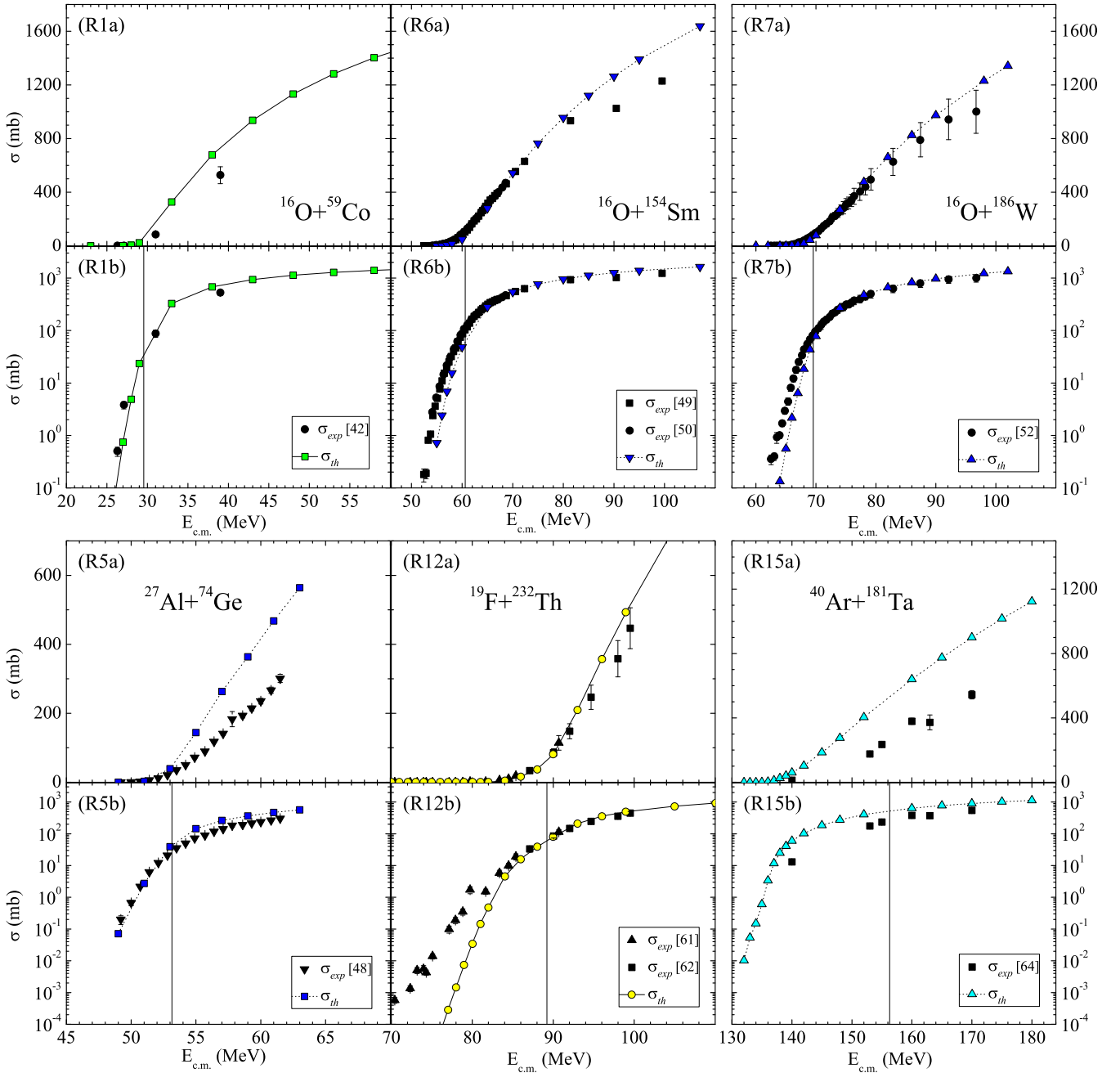
FIG. 6. Calculated and experimental cross sections as the functions of collision energy for six reactions. The values of $B_{\delta s}$ are displayed by vertical lines. For convenience, we use the ordering numbers of reactions from Table IV.

VII. CONCLUSIONS

For calculating the heavy-ion capture cross sections, in our previous works [8,29], we successfully employed the double-folding model with the M3Y NN forces. Recently, there appeared articles [15,16] in which the RMF NN forces were used for the same purpose. In Ref. [15], it is stated that the RMF forces provide better results in comparison with the M3Y ones. In the present paper, we intended to verify this statement.

For this aim, we have performed the systematic calculations of the capture cross sections for 20 asymmetric reactions

with deformed target nuclei in a wide range of the barrier energies (34–206 MeV). To account for the density dependence of the M3Y NN forces, we have developed an algorithm for modifying the strength of the zero-range density-independent exchange forces. The nucleus-nucleus interaction energy has been calculated by means of the double-folding model with the nucleon densities based on the experimental charge densities. This algorithm has been validated in Sec. VI B and applied for finding the SnnP, barrier energies, and curvatures. Then, we have evaluated the transmission coefficients within the framework of the single barrier penetration model for different incident angles.
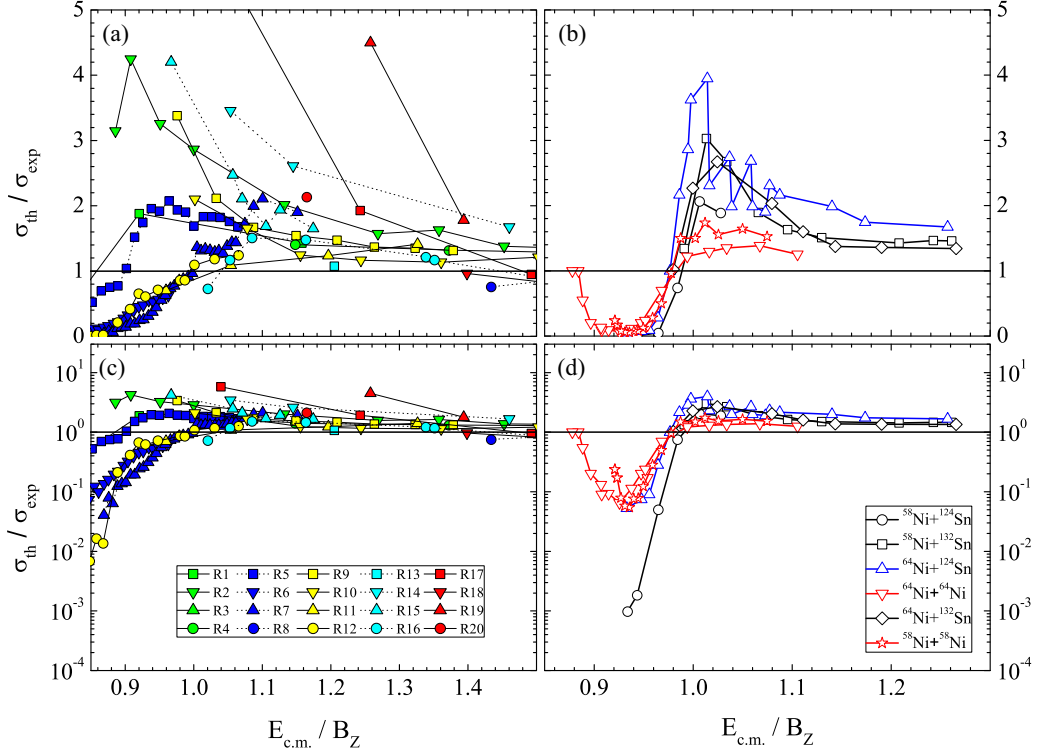
FIG. 7. Ratios of calculated cross-sections σ_{th} and experimental σ_{exp} as the functions of $E_{c.m.}/B_Z$. Panels (a) and (c) correspond to our M3Y calculations; panels (b) and (d) are based on the RMF calculations from [15] (the data are read from the figures of Ref. [15]). For convenience, we use the ordering numbers of reactions from Table IV.

The calculated cross sections have been compared quantitatively (i.e., point by point) with the experimental ones in Figs. 7(a) and 7(c). The same has been made in Figs. 7(b) and 7(d) using the results of Ref. [15] (the data are read from the figures of Ref. [15]). It has turned out that the amount of agreement, i.e., the ratios $\sigma_{th}(M3Y)/\sigma_{exp}$ and $\sigma_{th}(RMF)/\sigma_{exp}$, is approximately the same. Moreover, our present analysis demonstrates that the level of agreement between σ_{th} and σ_{exp} might be improved by accounting for the dissipative character of the collision process above the barrier.

APPENDIX

Here we present details of the calculations using the code DFMDEF. For the geometry of Fig. 1, Eq. (1) becomes

$$U_n(R, \theta) = U_{nD}(R, \theta) + U_{nE}(R, \theta). \tag{A1}$$

The direct part is evaluated using the Fourier transform and expanding in spherical harmonics (remember, that the density dependence absents here, i.e., $F(\rho_{FA}) = 1$ in Eqs. (2) and (6)),

$$U_{nD}(R, \theta) = \sum_{l=0,2,\dots}^{10} U_{nDl}(R) Y_{l0}(\theta), \tag{A2}$$

$$U_{nDl}(R) = \frac{4}{\sqrt{\pi}} \int_0^{k_{max}} dk\, k^2 j_l(kR) \tilde{v}_D(k) \tilde{A}_{PA0}(k) \tilde{A}_{TAl}(k), \tag{A3}$$

$$\tilde{A}_{P(T)Al}(k) = \int_0^{r_{max}} dr\, r^2 \rho_{P(T)Al}(r) j_l(kr), \tag{A4}$$

$$\rho_{P(T)Al}(r) = 2\pi \int_0^{\pi} d\zeta\, \sin(\zeta) \rho_{P(T)A}(r, \zeta) Y_{l0}(\zeta), \tag{A5}$$

$$\tilde{v}_D(k) = 4\pi \sum_{i=1}^{2} \frac{G_{Di} r_{vi}}{k^2 + r_{vi}^{-2}}. \tag{A6}$$

For evaluating the exchange part, we apply Eqs. (6)–(10). Finally, in the code the following equations are used:

$$U_{nEf}(R, \theta) = 4\pi \int_0^{s_{max}} ds\, s^2 j_0(k_{rel}s) v_{Ef}(s) G(R, s, \theta), \tag{A7}$$

$$G(R, s, \theta) = \int_0^{q_{max}} dq\, q^2 \int_0^{\pi} d\zeta\, h_P(R, s, q, \zeta, \theta) \\ \times h_T(R, s, q, \zeta, \theta) \sin(\zeta), \tag{A8}$$

$$h_P(R,\ s,\ q,\ \zeta,\ \theta) = \int_0^{2\pi} d\varphi\, \rho_{PA}(p) \tilde{j}_1[k_{Peff}(p)s], \tag{A9}$$

$$h_T(R,\ s,\ q,\ \zeta,\ \theta) = \rho_{TA}(q,\ \zeta) \tilde{j}_1[k_{Teff}(q,\ \zeta)s]. \tag{A10}$$

The values of k_{rel}, $\tilde{j}_1$, and $k_{P(T)eff}$ are determined by Eqs. (12), (9), and (10), respectively. Here we denoted $\vec{q} = \vec{r}_T - \vec{s}/2$ and $\vec{p} = \vec{r}_P + \vec{s}/2$ (see Fig. 1). The absolute value of the last vector

is equal to

$$p(R, q, \zeta, \varphi, \theta) = |\vec{q} - \vec{R}|$$
$$= [q^2 + R^2 + 2Rq(\sin\theta \sin\zeta \cos\varphi - \cos\theta \cos\zeta)]^{1/2}. \tag{A11}$$

The upper limits of integration are $r_{max} = s_{max} = q_{max} = 3R_{FT}$, $k_{max} = 5 \text{ fm}^{-1}$.

In the case of the zero-range exchange part of the *NN* interaction, Eq. (6) due to the Fourier transform reduces to the form similar to Eq. (A2) with

$$U_{nE\delta l}(R) = \frac{4}{\sqrt{\pi}} \int_0^{k_{max}} dk \, k^2 j_0(kR) G_{E\delta} \tilde{A}_{PA0} \tilde{A}_{TAl}. \tag{A12}$$

Note that for the deformed case the density dependence is not applicable.

---

[1] G. R. Satchler and W. G. Love, Phys. Rep. **55**, 183 (1979).

[2] G. W. Greenlees, G. J. Pyle, and Y. C. Tang, Phys. Rev. **171**, 1115 (1968).

[3] A. B. Migdal, *Theory of Finite Fermi Systems and Application to Atomic Nuclei* (Interscience, New York, 1967).

[4] B. Sinha, Phys. Rev. Lett. **33**, 600 (1974).

[5] G. R. Satchler, Nucl. Phys. **A329**, 233 (1979).

[6] M. Ismail and K. A. Ramadan, J. Phys. G: Nucl. Part. Phys. **26**, 1621 (2000).

[7] M. Rahmat and M. Modarres, Phys. Rev. C **97**, 034611 (2018).

[8] M. V. Chushnyakova, M. Bhuyan, I. I. Gontchar, and N. A. Khmyrova, Nucl. Phys. **A994**, 121657 (2020).

[9] V. V. Sargsyan, Z. Kanokov, G. G. Adamian, and N. V. Antonenko, Phys. Part. Nucl. **41**, 175 (2010).

[10] G. Bertsch, J. Borysowicz, H. McManus, and W. G. Love, Nucl. Phys. **A284**, 399 (1977).

[11] N. Anantaraman, H. Toki, and G. F. Bertsch, Nucl. Phys. **A398**, 269 (1983).

[12] I. I. Gontchar, D. J. Hinde, M. Dasgupta, and J. O. Newton, Phys. Rev. C **69**, 024610 (2004).

[13] I. I. Gontchar and M. V. Chushnyakova, Phys. At. Nucl. **79**, 543 (2016).

[14] I. I. Gontchar and M. V. Chushnyakova, J. Phys. G: Nucl. Part. Phys. **43**, 045111 (2016).

[15] M. Bhuyan and R. Kumar, Phys. Rev. C **98**, 054610 (2018).

[16] M. Bhuyan, R. Kumar, S. Rana, D. Jain, S. K. Patra, and B. V. Carlson, Phys. Rev. C **101**, 044603 (2020).

[17] M. V. Chushnyakova, I. I. Gontchar, and N. A. Khmyrova, J. Phys. G: Nucl. Part. Phys. **48**, 015101 (2021).

[18] D. T. Khoa, G. R. Satchler, and W. von Oertzen, Phys. Rev. C **56**, 954 (1997).

[19] A. M. Kobos, B. A. Brown, R. Lindsay, and G. R. Satchler, Nucl. Phys. **A 425**, 205 (1984).

[20] J. W. Negele and D. Vautherin, Phys. Rev. C **5**, 1472 (1972).

[21] X. Campi and A. Bouyssy, Phys. Lett. B **73**, 263 (1978).

[22] D. T. Khoa, W. von Oertzen, and H. G. Bohlen, Phys. Rev. C **49**, 1652 (1994).

[23] J. Cook, Comput. Phys. Commun. **25**, 125 (1982).

[24] I. I. Gontchar and M. V. Chushnyakova, Comput. Phys. Commun. **181**, 168 (2010).

[25] D. T. Khoa and W. von Oertzen, Phys. Lett. B **304**, 8 (1993).

[26] D. T. Khoa, Phys. Rev. C **63**, 034007 (2001).

[27] M. V. Chushnyakova and I. I. Gontchar, Phys. Rev. C **87**, 014614 (2013).

[28] I. I. Gontchar, R. Bhattacharya, and M. V. Chushnyakova, Phys. Rev. C **89**, 034601 (2014).

[29] M. V. Chushnyakova, R. Bhattacharya, and I. I. Gontchar, Phys. Rev. C **90**, 017603 (2014).

[30] P.-G. Reinhard, M. Rufa, J. Maruhn, W. Greiner, and J. Friedrich, Z. Phys. A: At. Nucl. **323**, 13 (1986).

[31] J. D. Walecka, The equation of state of nuclear matter and properties of finite nuclei in a relativistic Quantum field theory, in *Nuclear Interactions*, edited by B. A. Robson, Lecture Notes in Physics Vol. 92 (Springer Berlin/Heidelberg, 1976), pp. 294–305.

[32] B. Singh, S. K. Patra, and R. K. Gupta, in *Proceedings of the DAE Symposium on Nuclear Physics* (BRNS, Mumbai, India, 2010), Vol. 55, p. 200.

[33] C. Lahiri, S. K. Biswal, and S. K. Patra, Int. J. Mod. Phys. E **25**, 1650015 (2016).

[34] I. I. Gontchar, M. V. Chushnyakova, and N. A. Khmyrova, Comput. Phys. Commun. **259**, 107690 (2021).

[35] I. I. Gontchar and M. V. Chushnyakova, Comput. Phys. Commun. **222**, 414 (2018).

[36] I. I. Gontchar and M. V. Chushnyakova, Comput. Phys. Commun. **184**, 172 (2013).

[37] I. I. Gontchar, D. J. Hinde, M. Dasgupta, C. R. Morton, and J. O. Newton, Phys. Rev. C **73**, 034610 (2006).

[38] H. De Vries, C. W. De Jager, and C. De Vries, At. Data Nucl. Data Tables **36**, 495 (1987).

[39] V. I. Zagrebaev, A. S. Denikin, A. V. Karpov, A. P. Alekseev, M. A. Naumenko, V. A. Rachkov, V. V. Samarin, and V. V. Saiko, Nucl. Instruments Methods Phys. Res., Sect. A **859**, 112 (2017).

[40] P. Möller, A. J. Sierk, T. Ichikawa, and H. Sagawa, At. Data Nucl. Data Tables **109–110**, 1 (2016).

[41] L. H. Chien, D. T. Khoa, D. C. Cuong, and N. H. Phuc, Phys. Rev. C **98**, 064604 (2018).

[42] P. R. S. Gomes, T. J. P. Penna, E. F. Chagas, R. Liguori Neto, J. C. Acquadro, P. R. Pascholati, E. Crema, C. Tenreiro, N. Carlin Filho, and M. M. Coimbra, Nucl. Phys. **A534**, 429 (1991).

[43] L. Kowalski, J. C. Jodogne, and J. M. Miller, Phys. Rev. **169**, 894 (1968).

[44] L. C. Chamon, D. Pereira, E. S. Rossi, C. P. Silva, G. R. Razeto, A. M. Borges, L. C. Gomes, and O. Sala, Phys. Lett. B **275**, 29 (1992).

[45] D. Pereira, G. Ramirez, O. Sala, L. C. Chamon, C. A. Rocha, J. C. Acquadro, and C. Tenreiro, Phys. Lett. B **220**, 347 (1989).

[46] Y. Nagame, H. Nakahara, K. Sueki, H. Kudo, I. Kohno, and M. Yanokura, Z. Phys. A: At. Nucl. **317**, 31 (1984).

[47] D. Singh, R. Ali, M. Afzal Ansari, B. S. Tomar, M. H. Rashid, R. Guin, and S. K. Das, Phys. Rev. C **83**, 054604 (2011).

[48] E. F. Aguilera, J. J. Vega, J. J. Kolata, A. Morsad, R. G. Tighe, and X. J. Kong, Phys. Rev. C **41**, 910 (1990).

[49] J. R. Leigh, M. Dasgupta, D. J. Hinde, J. C. Mein, C. R. Morton, R. C. Lemmon, J. P. Lestone, J. O. Newton, H. Timmers, J. X. Wei, and N. Rowley, Phys. Rev. C **52**, 3151 (1995).

[50] U. Jahnke, H. H. Rossner, D. Hilscher, and E. Holub, Phys. Rev. Lett. **48**, 17 (1982).

[51] J. O. Newton, R. D. Butt, M. Dasgupta, D. J. Hinde, I. I. Gontchar, C. R. Morton, and K. Hagino, Phys. Rev. C **70**, 024605 (2004).

[52] M. Trotta, A. M. Stefanini, S. Beghini, B. R. Behera, A. Y. Chizhov, L. Corradi, S. Courtin, E. Fioretto, A. Gadea, P. R. S. Gomes, F. Haas, I. M. Itkis, M. G. Itkis, G. N. Kniajeva, N. A. Kondratiev, E. M. Kozulin, A. Latina, G. Montagnoli, I. V. Pokrovsky, N. Rowley, R. N. Sagaidak, F. Scarlassara, A. Szanto de Toledo, S. Szilner, V. M. Voskressensky, and Y. W. Wu, Eur. Phys. J. A **25**, 615 (2005).

[53] H. Gauvin, D. Guerreau, Y. Le Beyec, M. Lefort, F. Plasil, and X. Tarrago, Phys. Lett. B **58**, 163 (1975).

[54] H. Ikezoe, N. Shikazono, Y. Nagame, Y. Sugiyama, Y. Tomita, K. Ideno, I. Nishinaka, B. J. Qi, H. J. Kim, A. Iwamoto, and T. Ohtsuki, Phys. Rev. C **46**, 1922 (1992).

[55] R. J. Charity, J. R. Leigh, J. J. M. Bokhorst, A. Chatterjee, G. S. Foote, D. J. Hinde, J. O. Newton, S. Ogaza, and D. Ward, Nucl. Phys. A **457**, 441 (1986).

[56] A. L. Caraley, B. P. Henry, J. P. Lestone, and R. Vandenbosch, Phys. Rev. C **62**, 054612 (2000).

[57] H. Ikezoe, N. Shikazono, Y. Nagame, Y. Sugiyama, Y. Tomita, K. Ideno, A. Iwamoto, and T. Ohtsuki, Phys. Rev. C **42**, 342 (1990).

[58] W. Q. Shen, J. Albinski, A. Gobbi, S. Gralla, K. D. Hildenbrand, N. Herrmann, J. Kuzminski, W. F. J. Müller, H. Stelzer, J. Tke, B. B. Back, S. Bjrnholm, and S. P. Srensen, Phys. Rev. C **36**, 115 (1987).

[59] B. B. Back, R. R. Betts, J. E. Gindler, B. D. Wilkins, S. Saini, M. B. Tsang, C. K. Gelbke, W. G. Lynch, M. A. McMahan, and P. A. Baisden, Phys. Rev. C **32**, 195 (1985).

[60] J. Tõke, R. Bock, G. X. Dai, A. Gobbi, S. Gralla, K. D. Hildenbrand, J. Kuzminski, W. F. J. Müller, A. Olmi, H. Stelzer, B. B. Back, and S. Bjørnholm, Nucl. Phys. A **440**, 327 (1985).

[61] D. M. Nadkarni, A. Saxena, D. C. Biswas, R. K. Choudhury, S. S. Kapoor, N. Majumdar, and P. Bhattacharya, Phys. Rev. C **59**, R580 (1999).

[62] S. Kailas, A. Navin, A. Chatterjee, P. Singh, R. K. Choudhury, A. Saxena, D. M. Nadkarni, S. S. Kapoor, V. S. Ramamurthy, B. K. Nayak, and S. V. Suryanarayana, Phys. Rev. C **43**, 1466 (1991).

[63] R. Yanez, W. Loveland, J. S. Barrett, L. Yao, B. B. Back, S. Zhu, and T. L. Khoo, Phys. Rev. C **88**, 014606 (2013).

[64] H.-G. Clerc, J. G. Keller, C.-C. Sahm, K.-H. Schmidt, H. Schulte, and D. Vermeulen, Nucl. Phys. A **419**, 571 (1984).

[65] D. Logan, H. Delagrange, M. F. Rivet, M. Rajagopalan, J. M. Alexander, M. Kaplan, M. S. Zisman, and E. Duek, Phys. Rev. C **22**, 1080 (1980).

[66] Z. Zheng, B. Borderie, D. Gardes, H. Gauvin, F. Hanappe, J. Peter, M. F. Rivet, B. Tamain, and A. Zaric, Nucl. Phys. A **422**, 447 (1984).

[67] C. Ngô, J. Péter, B. Tamain, M. Berlanger, and F. Hanappe, Z. Phys. A: At. Nucl. **283**, 161 (1977).

[68] B. Tamain, C. Ngô, J. Péter, and F. Hanappe, Nucl. Phys. A **252**, 187 (1975).

[69] J. R. Birkelund, A. D. Hoover, J. R. Huizenga, W. U. Schröder, and W. W. Wilcke, Phys. Rev. C **27**, 882 (1983).

[70] M. A. Butler, S. S. Datta, R. T. de Souza, J. R. Huizenga, W. U. Schröder, J. Tõke, and J. L. Wile, Phys. Rev. C **34**, 2016 (1986).

[71] M. Dasgupta, D. J. Hinde, N. Rowley, and A. M. Stefanini, Annu. Rev. Nucl. Part. Sci. **48**, 401 (1998).

[72] J. O. Newton, C. R. Morton, M. Dasgupta, J. R. Leigh, J. C. Mein, D. J. Hinde, H. Timmers, and K. Hagino, Phys. Rev. C **64**, 064608 (2001).

[73] D. H. E. Gross and H. Kalinowski, Phys. Rep. **45**, 175 (1978).

[74] P. Fröbrich, Phys. Rep. **116**, 337 (1984).

[75] R. A. Kuzyakin, V. V. Sargsyan, G. G. Adamian, and N. V. Antonenko, Phys. Part. Nucl. **48**, 158 (2017).

[76] V. Zagrebaev and W. Greiner, J. Phys. G: Nucl. Part. Phys. **34**, 1 (2007).